석 사 학 위 논 문

Master's Thesis

동심 원형 능동센서를 이용한 유도파의 모드 분해 기법

Lamb Wave Mode Decomposition using Concentric Ring and Circular PZT Transducers

염 철 민 (廉 哲 旼 **Yeum, Chulmin**)

건설 및 환경공학과

Department of Civil and Environmental Engineering

한 국 과 학 기 술 원

Korea Advanced Institute of Science and Technology

2010

동심 원형 능동센서를 이용한 유도파의 모드 분해 기법

Lamb Wave Mode Decomposition using Concentric Ring and Circular PZT Transducers

Lamb Wave Mode Decomposition using Concentric Ring and Circular PZT Transducers

Advisor : Professor **Hoon Sohn**

by

Chulmin Yeum

Department of Civil and Environmental Engineering
Korea Advanced Institute of Science and Technology

A thesis submitted to the faculty of the Korea Advanced Institute of Science and Technology in partial fulfillment of the requirements for the degree of Master of Engineering in the Department of Civil and Environmental Engineering.

Daejeon, Korea
2010. 06. 05.
Approved by

_____

Professor **Hoon Sohn**
Major Advisor

동심 원형 능동센서를 이용한 유도파의 모드 분해 기법

염 철 민

위 논문은 한국과학기술원 석사학위논문으로 학위논문 심사위원회에서 심사 통과하였음.

2010 년 06 월 05 일

심사 위원장 손   훈 (인)

심 사 위 원 명   현 (인)

심 사 위 원 정 형 조 (인)

ABSTRACT

Lamb waves using surface-bonded piezoelectric transducers (PZTs) have been widely used for nondestructive testing (NDT). However, the identification of individual Lamb wave modes and the subsequent data interpretation are often difficult due to the dispersive and multimodal natures of Lamb waves. To tackle the problem, a new Lamb wave mode decomposition technique using concentric ring and circular PZTs is proposed. Its advantages over the conventional approaches are that (1) PZTs need to be placed only a single surface of a specimen and (2) mode decomposition can be performed at any desired frequency without changing the PZT size and/or spacing configuration. The proposed mode decomposition technique is formulated by solving 3D Lamb wave propagation equations considering the PZT size and shape, and this technique requires a specially designed dual PZT composed of concentric ring and circular PZTs. The effectiveness of the proposed technique for the Lamb wave mode decomposition is investigated through numerical simulation and experimental tests performed on an aluminum plate.

TABLE OF CONTENTS

ACKNOWLEDGEMENTS (IN KOREAN)

CURRICULUM VITAE

LIST OF FIGURES

CHAPTER 1
INTRODUCTION

1.1 Motivation

Lamb waves have gained a great deal of attention for structural health monitoring (SHM) and nondestructive testing (NDT) of plate-like structures.[1-6] Lamb waves are mechanical waves whose wavelength is in the same order of magnitude as the thickness of the plate. One of the main advantages of Lamb waves is that they can travel considerable distances with little attenuation, allowing the inspection of large areas. However, the analysis and interpretation of Lamb waves can be complicated due to their dispersive and multimodal natures. The various frequency components of Lamb waves travel at different speeds, causing the shape distortion of wave packets. Furthermore, there exit multiple modes, at least two modes, at any specific driving frequency, making subsequent signal interpretation challenging.

1.2 Literature review

To ease the analysis and interpretation of Lamb waves, selective Lamb wave generation and sensing have been investigated. Examples of the selective Lamb wave generation and sensing techniques include (1) angle wedge tuning using contact and non-contact type wedge transducers,[13-14] (2) wavelength-matched linear arrays, using comb transducers,[15-16] and (3) point source point receiver (PS-PR) using Hertzian contacts and non-contact laser beams.[17-18] However, these conventional techniques have drawbacks and limitations. Some of conventional transducers may be too heavy and bulky for online monitoring of structures such as airplanes and have directionality for selective Lamb wave mode generation and sensing. Furthermore, due to their relatively high cost, they are not suitable for deployment to large-scale structures. Lastly, some parameters of the transducer such as the incidence angle of the wedge transducer or the element spacing of the comb transducer need to be manually adjusted for selective Lamb wave excitation and sensing at a different frequency.

Recently, embedded or surfaced-bonded PZTs are used to overcome some of the conventional transducers' drawbacks. In particular, the use of piezoelectric wafer transducers (hereafter, PZTs) is becoming popular for online SHM due to their light weight, unobtrusive nature, and low cost.[7-12] Mode isolation techniques using PZTs include (1) placement of collocated PZTs on both surfaces of a specimen,[19] (2) an array of PZTs with time delays,[20] and (3) tuning of the driving frequency and/or the PZT size for a specific mode excitation and sensing.[21-22] For

the collocated PZT technique, access to both surfaces of a structure can be limited, and precise placement of collocated PZTs can be challenging. The PZT array technique requires a multi-channel data acquisition system and precise control of prescribed time delay profiles. For the tuning technique, the isolation of a single Lamb mode is possible only at a specific frequency where the target mode is predominant or by tuning the PZT size to match with the half of the target mode's wavelength. That is, the mode selection is possible only at a specific frequency and for a fixed PZT size.

1.3 Contribution and uniqueness

In this study, a new Lamb wave mode decomposition technique is proposed so that fundamental symmetric (S_0) and anti-symmetric (A_0) modes can be decoupled at an arbitrary driving frequency without adjustment of the PZT size. First, the response models of circular and ring shape PZTs are derived, and the proposed mode decomposition technique is formulated based on the response model of a dual PZT, that is composed of concentric ring and circular PZTs. Then, numerical simulation and experimental tests are executed to investigate the feasibility of the proposed technique. The advantages of the proposed technique are that (1) PZTs need to be placed only a single surface of the structure, (2) mode decomposition can be performed at any desired frequency without physical adjustment of the PZT size and/or spacing, (3) both S_0 and A_0 modes can be simultaneously decoupled and identified at any driving frequency, and (4) a circular design of the dual PZT allows omni-directional Lamb wave decomposition.

CHAPTER 2
THEORETICAL FORMULATION

2.1 Introduction

The proposed mode decomposition technique decouples fundamental Lamb wave (S_0 and A_0) modes from measured signals without PZT size adjustment or frequency tuning. The basic premise behind the proposed technique is that the amplitudes of the S_0 and A_0 modes change at "different" rates, as the sizes of the excitation and sensing PZTs vary. Based on this premise, a new "dual" PZT composed of co-centered circular and ring PZTs is designed and the mode decomposition is realized by manipulating multiple signals measured by activating different parts of the dual PZTs for excitation and sensing. Because the proposed technique can decompose only the S_0 and A_0 modes, the applicable frequency range is limited below the cutoff frequencies of the A_1 or S_1 modes.

This section is organized as follow. First, an analytical solution of the Lamb wave response at a surface bonded circular PZT is derived. Next, a newly designed dual PZT is introduced, and a Lamb wave decomposition technique using the dual PZT is developed. Finally, a procedure to estimate the normalized scaling factors, necessary for the proposed decomposition technique, from measured signals is described.

2.2 Analytical solution of the Lamb wave response at a circular PZT
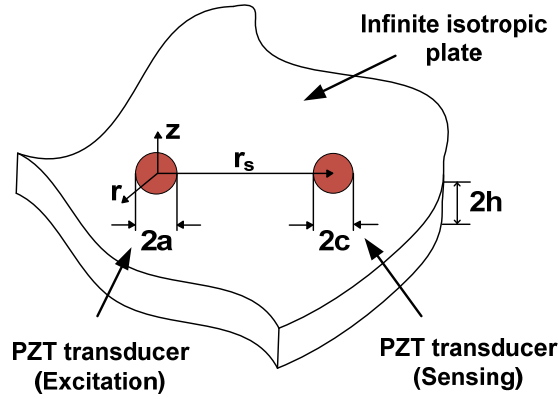
Figure 2.1 Two circular PZTs bonded on a surface of an infinite isotropic plate

First, the analytical displacement response at an arbitrary distance from an exciting circular PZT is presented. Figure 2.1 presents an isotropic plate with one pair of exciting and sensing circular PZTs bonded on a single surface. Assuming that the exciting circular PZT is located at the origin of a polar coordinate system (r=0) and it produces axisymmetric circular waves, the circumferential displacement (u_θ) and the derivative with respect to θ ($\partial/\partial\theta$) become zero. When the excitation PZT is assumed to be perfectly bonded to the plate, the excitation can be modeled using the 'pin-force model' that only produces surface shear stress around its circumference boundary. Then, the shear stress at a specific excitation frequency ω becomes $\tau_{zr} = \tau_0 \delta(r-a) \cdot e^{i\varpi t}$. Here, δ is the Dirac delta function and τ_0 is the amplitude of the generated shear stress. The radial displacement (u_r) at a distance of r from the exciting circular PZT becomes:[7]

$$u_r(r, z = h) = -\pi i \frac{\tau_0 a}{\mu} e^{i\omega t} \cdot \left[\begin{array}{l} \sum_{\xi^S} J_1(\xi^S a) \dfrac{N_S(\xi^S)}{D_S{}'(\xi^S)} H_1^{(2)}(\xi^S r) \\ \\ + \sum_{\xi^A} J_1(\xi^A a) \dfrac{N_A(\xi^A)}{D_A{}'(\xi^A)} H_1^{(2)}(\xi^A r) \end{array} \right] \qquad (2.1)$$

where $\alpha^2 = \dfrac{\omega^2}{c_L{}^2} - \xi^2$, $\beta^2 = \dfrac{\omega^2}{c_T{}^2} - \xi^2$, $c_L = \sqrt{\dfrac{\lambda + 2\mu}{\rho}}$, $c_T = \sqrt{\dfrac{\mu}{\rho}}$,

$$N_S = \xi\beta(\xi^2 + \beta^2)\cos\alpha b \cos\beta b,$$

$$D_S = (\xi^2 - \beta^2)^2 \cos\alpha b \sin\beta b + 4\xi^2\alpha\beta \sin\alpha b \cos\beta b,$$

$$N_A = \xi\beta(\xi^2 + \beta^2)\sin\alpha b \sin\beta b,$$

$$D_A = (\xi^2 - \beta^2)^2 \sin\alpha b \cos\beta b + 4\xi^2\alpha\beta \cos\alpha b \sin\beta b.$$

λ and μ are Lame constants for the plate material, and ρ is the material density of the plate. The superscripts or subscripts S and A denote the symmetric and antisymmetric Lamb modes, respectively. The wavenumber ξ of a specific mode at a given ω is obtained by solving the Rayleigh-Lamb equation of an isotropic plate.[15] $J_1()$ is the Bessel function of the first kind of order 1, and $H_1^{(2)}()$ is the Hankel function of order 1 of the second type.

Next, the voltage response of a circular sensing PZT is calculated by integrating the strain field over the entire area of the sensing PZT and considering the piezoelectricity of the sensing PZT. The deformation of the sensing PZT creates charge (Q_P), and the output voltage (V) at the sensing PZT is obtained by dividing the charge by the PZT capacitance value (C_p):

$$V(t) = \frac{Q_P}{C_P} = \frac{E_s h_s g_{31}}{A} \int_A \varepsilon_{kk} dA \tag{2.2}$$

where E_S, h_S and A are Young's modulus, thickness, and surface area of the sensing PZT, respectively. g_{31} is the xz-directional piezoelectric voltage constant and ε_{kk} is the sum of the in-plane extensional surface strains. When the shape of the sensing PZT is circular, the area integral in Equation (2.2) becomes[7]

$$V(t) = \frac{E_s h_s g_{31}}{A} \iint_A \left(\varepsilon_{rr} + \varepsilon_{\theta\theta} \right) r dr d\theta = \frac{E_s h_s g_{31}}{A} \iint_A \left(\frac{du_r}{dr} + \frac{u_r}{r} \right) r dr d\theta \tag{2.3}$$

Because of the axisymmetric nature of the wave propagations, all u_θ and $\partial/\partial\theta$ terms vanish and only ε_{rr} and $\varepsilon_{\theta\theta}$ terms remain. By substituting the radial displacement in Equation (2.1) into Equation (2.3), the output voltage at the sensing PZT becomes

$$V(t) = -i \frac{\tau_0 E_s h_s g_{31} a}{\mu c^2} e^{i\omega t} \left[\begin{array}{c} \sum_{\xi^S} J_1\left(\xi^S a\right) \dfrac{N_S\left(\xi^S\right)}{D_S'\left(\xi^S\right)} \iint_A \xi^S r H_0^{(2)}\left(\xi^S r\right) dr d\theta \\ + \sum_{\xi^A} J_1\left(\xi^A a\right) \dfrac{N_A\left(\xi^A\right)}{D_A'\left(\xi^A\right)} \iint_A \xi^A r H_0^{(2)}\left(\xi^A r\right) dr d\theta \end{array} \right] \tag{2.4}$$

where $H_0^{(2)}(\ )$ is the complex Hankel function of order 0 of the second type. Equation (2.4) can be further simplified by assuming that (1) the distance between the excitation and sensing PZTs is much longer compared to the size of the sensing PZT and (2) the complex Hankel function shows an asymptotic behavior after four or five cycles of the wavelength of the excited mode.[23]
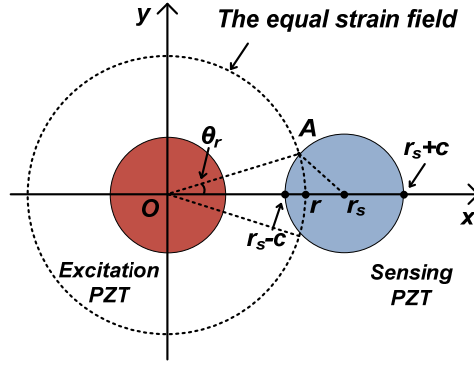
Figure 2.2 The response calculation of a circular sensing PZT with the center at $(r_s,0)$ and radius c when Lamb waves are generated by a circular excitation PZT with a radius r at the origin of the coordinate. The dash line represents the equal strain field generated by the circular excitation PZT.

Figure 2.2 shows the circular excitation PZT positioned at the origin and the other sensing PZT centered at $(r_s,0)$. The dotted circular represents the equal strain field generated from the edge of the excitation PZT. The output voltage of the sensing PZT can be obtained by integrating the strain field over the entire sensing area and by multiplying it with the constants shown in Equation (2.2).

First, θ_r in Figure 2.2 is represented as a function of c, r_s and r. In Figure 2.2, point A is one of the intersections between the circular equal strain field (dotted circle) with a radius of r and the edge of the circular sensing PZT with a radius of c. θ_r is an angle between $\overline{OA}$ and x-axis. When the radius of the sensor (c) is small enough compared to the wave propagation distance (r), the higher order terms of the Maclaurin series of $\cos \cos \theta_r$ can be omitted and $\cos \theta_r \cong 1 - \theta_r^2 / 2$. Then, θ_r becomes:

$$\theta_r = \sqrt{\frac{c^2 - (r_s - r)^2}{r_s r}} \tag{2.5}$$

Next, the Hankel function can be approximated as follows using the fact that it exhibits an asymptotic behavior after four or five cycles of the wavelength of the mode considered:[23]

$$H_0^{(2)}(\xi r) \cong \sqrt{\frac{2}{\pi \xi r}} e^{i(\xi r - \frac{\pi}{4})} \tag{2.6}$$

By submitting Equations (2.5) and (2.6) into Equation (2.4), the output voltage becomes:

$$V(t) = -i \frac{2\tau_0 E_s h_s g_{31} a}{\mu c^2} \sqrt{\frac{2}{\pi r_s}} e^{i(\omega t - \frac{\pi}{4})} \cdot \tag{2.7}$$

$$\left[J_1\left(\xi^{S_0} a\right) \frac{N_S\left(\xi^{S_0}\right)}{D_S'\left(\xi^{S_0}\right)} \int_{r_s-c}^{r_s+c} \sqrt{\xi^{S_0}\{c^2 - (r_s - r)^2\}} \, e^{i\xi^{S_0} r} dr \right.$$

$$\left. + J_1\left(\xi^{A_0} a\right) \frac{N_A\left(\xi^{A_0}\right)}{D_A'\left(\xi^{A_0}\right)} \int_{r_s-c}^{r_s+c} \sqrt{\xi^{A_0}\{c^2 - (r_s - r)^2\}} \, e^{i\xi^{A_0} r} dr \right]$$

Note that only the fundamental symmetric (S_0) and antisymmetric (A_0) modes are included in Equation (2.7) without loss of generality.

Equation (2.7) can be further simplified using the Poisson integral of the Bessel function.[25]

$$J_n(z) = \left(\Gamma(n + \frac{1}{2}) \Gamma(\frac{1}{2}) \right)^{-1} (\frac{1}{2} z)^n \int_{-1}^{+1} (1 - t^2)^{n - \frac{1}{2}} e^{izt} dt \tag{2.8}$$

where $\Gamma(\ )$ is the Gamma function. Finally, the output voltage of the circular sensing PZT with a radius of c corresponding to the other circular PZT excitation

with a radius of *a* becomes:

$$V(t) = -i \frac{2\tau_0 E_s h_s g_{31} a \sqrt{2\pi}}{\mu c \sqrt{r_s}} \left[\begin{array}{l} \frac{1}{\sqrt{\xi^{S_0}}} J_1\left(\xi^{S_0} a\right) J_1\left(\xi^{S_0} c\right) \frac{N_s\left(\xi^{S_0}\right)}{D_s'\left(\xi^{S_0}\right)} e^{i\left(\omega t - \frac{\pi}{4} + \xi^{S_0} r_s\right)} \\[3mm] + \frac{1}{\sqrt{\xi^{A_0}}} J_1\left(\xi^{A_0} a\right) J_1\left(\xi^{A_0} c\right) \frac{N_s\left(\xi^{A_0}\right)}{D_s'\left(\xi^{A_0}\right)} e^{i\left(\omega t - \frac{\pi}{4} + \xi^{A_0} r_s\right)} \end{array} \right] \quad (2.9)$$

Equation (2.9) shows that given the driving frequency and the corresponding wavenumber of each mode, the arrival times of the S_0 and A_0 modes are controlled only by the distance between the sensing and excitation PZTs (r_s) and not affected by their sizes. On the other hand, the amplitudes of the S_0 and A_0 modes are functions of the excitation and sensing PZT sizes (*a* and *c*) as well as the geometrical attenuation due to 2D energy dissipation ($1/\sqrt{r_s}$). Thus, the terms in Equation (2.9) can be grouped into two categories: one controlled by r_s and the other controlled by *a* and *c*:

$$V(t) = C^{S_0}(r_s) S^{S_0}(a,c) + C^{A_0}(r_s) S^{A_0}(a,c) \quad (2.10)$$

where $\quad C^{S_0}(r_s) = -i \frac{2\sqrt{2\pi} \tau_0 E_s h_s g_{31}}{\mu \sqrt{\xi^{S_0} r_s}} \frac{N_s\left(\xi^{S_0}\right)}{D_s'\left(\xi^{S_0}\right)} e^{i\left(\omega t - \frac{\pi}{4} + \xi^{S_0} r_s\right)}$

$$S^{S_0}(a,c) = \frac{a}{c} J_1\left(\xi^{S_0} a\right) J_1\left(\xi^{S_0} c\right)$$

$C^{A_0}(r_s)$ and $\ S^{A_0}(a,c)\ $ are defined in a similar fashion.

Note that, because the S_0 and A_0 modes have different wavenumbers, these two modes have different amplitudes for the same excitation and sensing PZT sizes.

Furthermore, their amplitudes change at different rates as the sizes of the actuator and sensor vary.

Hypothetically assuming that all parameters are fixed except the actuator and/or sensor sizes, the multiple response signals can be measured by varying the actuator and sensor sizes. The values of $S^{S_0}(a,c)$ and $S^{A_0}(a,c)$ corresponding to varying actuator and sensor sizes can be analytically computed once the wavenumbers of the S_0 and A_0 modes are known. Then, $C^{S_0}(r_s)$ and $C^{A_0}(r_s)$ which are independent of actuator and sensor sizes can be estimated from multiple combinations of the response signals and $S^{S_0}(a,c)$ and $S^{A_0}(a,c)$. The main challenge in this approach is to vary only the sizes of the actuator and sensor without changing the other parameters in Equation (2.9) including r_s. This problem is addressed by designing a new dual PZT configuration described next subsection.

2.3 Description of a dual PZT

Before describing the proposed decomposition technique, the configuration of a dual PZT is introduced.[11, 26] Figure 2.3(a) illustrates the schematic drawing of the dual PZT. The dual PZT consists of concentric ring and circular PZTs. These two PZT components can be activated independently or simultaneous for Lamb wave excitation and sensing.
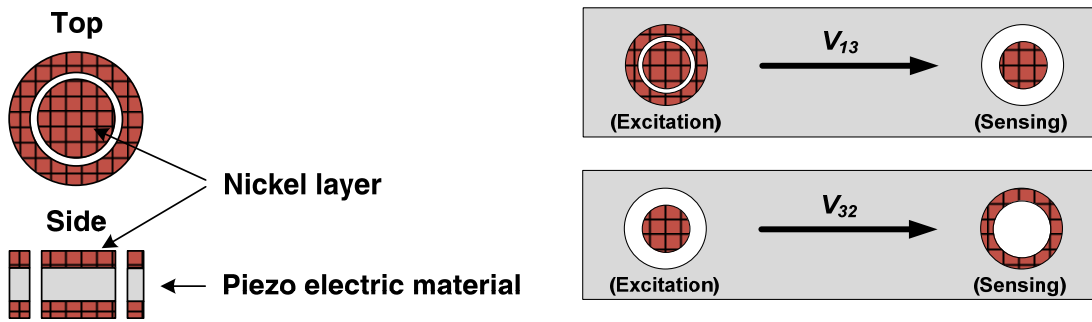
(a) A schematic of the dual PZT   (b) Signals obtained by dual PZTs

Figure 2.3 A schematic drawing of the dual PZT and examples of signals obtained by the dual PZTs: (a) The configuration of the dual PZT composed of co-centered ring and circular PZTs (b) V_{13} denotes a response measured by the inner circular part of the sensing PZT when both the outer ring and inner circular parts of the excitation PZT are activated. Similarly, V_{32} is measured by the ring part of the sensing PZT when the circular part of the excitation PZT is actuated. (Here, the subscripts, 1, 2 and 3 denote the entire dual PZT, the outer ring PZT and the inner circular PZT, respectively.) The darker (red) area of the dual PZT represents the PZT component(s) activated either for excitation or sensing.

By activating different parts of the excitation and sensing dual PZTs, nine

different response signals can be obtained: V_{ij}, i and j = 1, 2 and 3. Here, i and j denote the different part(s) of the dual PZT activated for excitation and sensing. 1, 2 and 3 represent the entire, ring and circular parts of the dual PZT, respectively. For example, V_{13} in Figure 2.3(b) represents the response signal measured by the circular part of the sensing dual PZT when both the ring and circular parts of the excitation dual PZT are actuated. V_{32} is defined in a similar manner. The darker (red) area(s) in Figure 2.3(b) show the PZT part(s) activated for Lamb wave excitation or sensing.

2.4 Formulation of a decomposition technique

Now using dual PZTs, multiple response signals can be obtained: V_{ij}, i and j = 1, 2 and 3. The theoretical response models for V_{ij} can be easily obtained from Equation (2.9) by slightly modifying the equation when the ring part of the dual PZT is used either for excitation or sensing. For example, the response model of a ring PZT sensor can be obtained by integrating the surface strain over the ring PZT area. This response model of the ring PZT can be equivalently obtained by subtracting the strain over a circular PZT, where its radius is same as the inner radius of the ring PZT, from the strain over another circular PZT with its radius equal to the outer radius of the ring PZT.

The radial displacement at a single point generated by a ring-shape PZT with outer and inner radii of a_1 and a_2 becomes:[23]

$$u_r(r, z = h) = -\pi i \frac{\tau_0}{\mu} e^{i\omega t} \cdot \left[\begin{array}{c} \sum_{\xi^S} \left(a_1 J_1\left(\xi^S a_1\right) - a_2 J_1\left(\xi^S a_2\right) \right) \dfrac{N_S\left(\xi^S\right)}{D_S^{'}\left(\xi^S\right)} H_1^{(2)}\left(\xi^S r\right) \\ + \sum_{\xi^A} \left(a_1 J_1\left(\xi^A a_1\right) - a_2 J_1\left(\xi^A a_2\right) \right) \dfrac{N_A\left(\xi^A\right)}{D_A^{'}\left(\xi^A\right)} H_1^{(2)}\left(\xi^A r\right) \end{array} \right] \quad (2.11)$$

where N_S (N_A) and D_S (D_A) are defined in Chapter 2.2. Basically, the response model generated by the ring PZT can be obtained by subtracting the response corresponding to the inner circle PZT with a radius of a_2 from that corresponding to the outer circular PZT with a radius of a_1.

The output voltage response at the ring sensing PZT can be obtained by integrating the surface strain in Equation (2.2) over the ring-shape of the sensing

PZT. Similar to the ring-shape excitation, the response of the ring-shape PZT is calculated by subtracting the strain over the inner circular area from the strain of the outer circular area.

Next, the relationships among various S_{ij}'s can be obtained using the following two superposition relationships. In the first superposition relationship, the summation of the response signals obtained by the individual excitations of the ring and circular PZTs is equal to the response obtained by the excitation of the entire PZT area for any fixed sensing PZT size:

$$V_{1j} = V_{2j} + V_{3j} \qquad \text{for} \quad j = 1 \sim 3 \qquad (2.12)$$

The other superposition relationship is established for the varying sensing PZT size. The output voltage obtained by the entire area of the dual PZT is the weight summation of the responses separately measured by the ring and circular PZTs, and the weight values are determined by the relative areas of the corresponding sensing PZT parts:

$$V_{i1} = \alpha V_{i2} + \beta V_{i3} \qquad \text{for} \quad i = 1 \sim 3 \qquad (2.13)$$

where $\alpha + \beta = 1$, and α and β are the ratios of the ring and circular PZT areas to the entire PZT area.

Based on the Equation (2.11) and two superposition relationships in Equations (2.12) and (2.13), all nine signals (V_{ij} for i, j = 1, 2 and 3) can be obtained as follow:

$$\mathbf{V = SC} \qquad (2.14)$$

where a_1, a_2 and a_3 are the outer and the inner radii of the ring PZT and the radius of the inner circular PZT, respectively,

$$\mathbf{V} = \begin{bmatrix} V_{11} \\ V_{12} \\ \vdots \\ V_{33} \end{bmatrix}, \quad \mathbf{S} = \begin{bmatrix} S_{11} & A_{11} \\ S_{12} & A_{12} \\ \vdots & \vdots \\ S_{33} & A_{33} \end{bmatrix}, \quad \mathbf{C} = \begin{bmatrix} C^{S_0}(r_s) \\ C^{A_0}(r_s) \end{bmatrix}$$

$$S_{33} = S^{S_0}(a_3, a_3)$$

$$S_{23} = S^{S_0}(a_1, a_3) - S^{S_0}(a_2, a_3)$$

$$S_{32} = (K_1 - K_2)^{-1}(K_1 S^{S_0}(a_3, a_1) - K_2 S^{S_0}(a_3, a_2)) \, ,$$

$$S_{22} = (K_1 - K_2)^{-1} \begin{bmatrix} K_1(S^{S_0}(a_1, a_1) - S^{S_0}(a_3, a_1)) \\ -K_2(S^{S_0}(a_1, a_2) - S^{S_0}(a_3, a_2)) \end{bmatrix} \, ,$$

$$S_{21} = (K_1 - K_2 + K_3)^{-1}\{(K_1 - K_2)S_{22} + K_3 S_{23}\} \, ,$$

$$S_{31} = (K_1 - K_2 + K_3)^{-1}\{(K_1 - K_2)S_{32} + K_3 S_{33}\} \, ,$$

$$S_{13} = S_{23} + S_{33} \, , \ S_{12} = S_{22} + S_{32} \, , \ S_{11} = S_{21} + S_{31} \ \, ,$$

$$K_j = \pi(a_j)^2 \, ,$$

A_{ij} are defined in a similar fashion using $S^{A_0}(a_i, a_j)$ and K_j.

S_{ij} and A_{ij} are defined as the scaling factors similar to $S^{S_0}(a, c)$ and $S^{A_0}(a, c)$ in Equation (2.10), and they depend only on the size of the PZT used. For example, S_{13} corresponds to the scaling factor when the entire dual PZT is activated for excitation and only the inner circular PZT is used for sensing.

The procedures of the proposed mode decomposition can be summarized as follows

(1) A total of nine V_{ij} are obtained by activating different parts (the outer ring, inner circle or both) of the excitation and sensing dual PZTs

(2) For the given sizes of the dual PZTs activated for excitation and sensing, the corresponding scaling factors can be analytically or experimentally

computed. The detailed procedure for the estimation of the scaling factor matrix **S** is described in the following section.

(3) The matrix **C** in Equation (2.14) can be estimated by taking the pseudo-inverse of the scaling factor matrix **S** and premultiply it to the matrix **V**. Because Equation (2.14) is an over-determined system, the estimated $C^{S_0}(r_s)$ and $C^{A_0}(r_s)$ are the optimal solution that minimizes the least squares errors.

(4) Finally, either the S_0 or A_0 mode in any measured signal can be decomposed and isolated. For example, the contribution of the S_0 mode in V_{13} can be obtained as $S_{13} \times C^{S_0}(r_s)$.

2.5 Estimation of the scaling factors from measured signals

The success of the proposed technique relies on the precise estimate of the scaling factor matrix $\mathbf{S}$ in Equation (2.14). Here, the scaling factor matrix can be analytically estimated similar to the computation of a Lamb wave tuning curve, which is the amplitude plots of symmetric and antisymmetric Lamb wave modes as a function of the driving frequency. However, a theoretical Lamb wave tuning curve obtained from the analytical Lamb wave propagation model do not necessarily match well with the experimental ones, because (1) the PZT is not fully coupled with the host structure due to bonding layer, (2) consequently, the effective PZT size becomes less than the physical PZT size, and (3) material properties of the structure continuously vary due to temperature and external loading.[24]

Alternatively, the scaling factors, more precisely the normalized scaling factors which will be introduced later, can be estimated solely from the measured response signals. Note that S_{ij} cannot be directly estimated from the measured V_{ij}. However, the amplitude of the S_0 mode $(S_{ij} \times C^{S_0}(r_s))$ in any V_{ij} can be easily estimated, and it can be shown that the ratio of the signed S_0 mode amplitude in V_{ij} to that in V_{11} is $(S_{ij} \times C^{S_0}(r_s))/(S_{11} \times C^{S_0}(r_s)) = S_{ij}/S_{11}$. Therefore, the normalized scaling factors for the S_0 mode, defined as $\tilde{S}_{ij} = S_{ij}/S_{11}$, can be readily obtained from the measured signals by computing the signed amplitude ratio of the S_0 mode in V_{ij} to that in V_{11}. Similarly, the normalized scaling factors for the A_0 mode can be defined as $\tilde{A}_{ij} = A_{ij}/A_{11}$ and obtained from V_{ij}. Now,

Equation (2.14) can be rearranged as follows:

$$
\begin{bmatrix} V_{11} \\ V_{12} \\ \vdots \\ V_{33} \end{bmatrix} = \begin{bmatrix} \tilde{S}_{11} & \tilde{A}_{11} \\ \tilde{S}_{12} & \tilde{A}_{12} \\ \vdots & \vdots \\ \tilde{S}_{33} & \tilde{A}_{33} \end{bmatrix} \begin{bmatrix} S_{11}C^{S_0} \\ A_{11}C^{A_0} \end{bmatrix} \tag{2.15}
$$

where $\tilde{S}_{ij} = S_{ij}/S_{11}$, $\tilde{A}_{ij} = A_{ij}/A_{11}$

The requirement is that the first arriving S_0 and A_0 modes are well separated in the time domain so that their signed amplitudes can be easily estimated. However, when the distance between the excitation and sensing PZTs is too short or there are multiple reflection paths, the estimation of the signed amplitudes of the first arriving S_0 and A_0 modes can be challenging.

This problem can be addressed by placing a pair of excitation and sensing PZTs with a longer spacing so that the first arrivals of the S_0 and A_0 modes can be well separated and the normalized scaling factors can be estimated from this longer path. Note that because the scaling factors as well as the normalized scaling factors are only functions of the wavenumbers and sizes of the actuator and sensor PZTs, they are independent of the spacing between the excitation and sensing PZTs. Therefore, the normalized scaling factors estimated from a single long path can be used for the mode decomposition in all the other paths with varying path lengths as long as they use the same sizes of the dual PZTs.

CHAPTER 3
NUMERICAL SIMULATION

3.1 Simulation setup

First, the proposed mode decomposition technique using dual PZTs was examined through numerical simulation. One of the commercially available finite element analysis (FEA) software programs (MSC/NASTRAN) and pre- and post-processor (PATRAN) was used for the simulation. For numerical simulation, a 3-D aluminum plate of 200 mm× 400 mm× 3 mm was simulated as shown in Figure 3.1. The PZT is assumed to be perfectly bonded on a structure and no damping is considered. The input force exerted by the excitation PZT is modeled as a 'pin-force' applied along its circumference boundary. The corresponding output response is computed by integrating the strain over the sensing PZT that is meshed on the structure as shown in Figure 3.2. Two dual PZTs were modeled on the top surface of the plate and the third dual PZT was modeled on the other side of the plate. PZT A and PZT C are located at the identical position but on the opposite side.
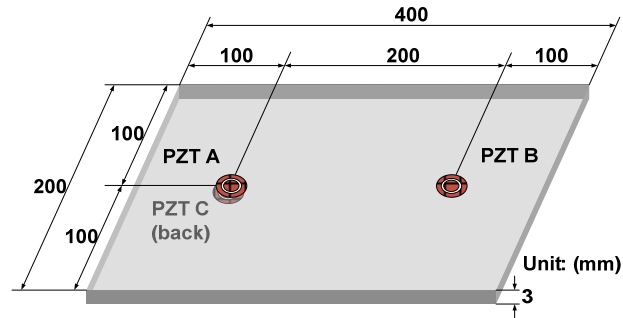
Figure 3.1 The dimension and configuration of the plate structure with the dual PZTs used for numerical simulation: PZT C is placed at the same position of PZT A but on the other side of the plate.

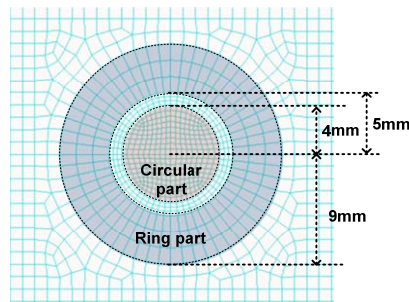Figure 3.2 The dimension of the dual PZT meshed on the surface of the structure

The driving frequency was selected to be 180 kHz so that only the S_0 and A_0 modes were generated and sensed. The maximum mesh size was 1mm× 1mm× 1mm, and the sampling rate was chosen to be sufficiently high to capture the smallest traveling wavelength. Rayleigh damping coefficients for the plate model were set to
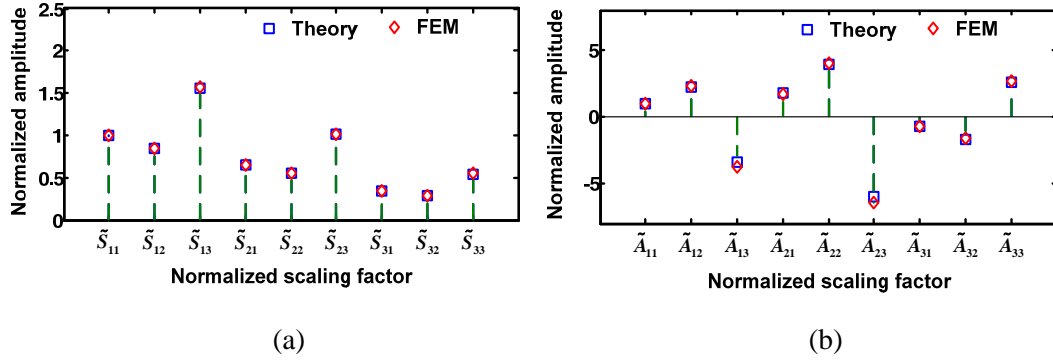
3.2 Simulation results

(a)   (b)

Figure 3.3 Comparison of the normalized scaling factors, $\tilde{S}_{ij}$ and $\tilde{A}_{ij}$, obtained from numerical simulation and theoretical solutions: the normalized scaling factors (a) for the S_0 mode and (b) for the A_0 mode. (The red rectangular and blue diamond indicate the theoretical and numerical normalized scaling factors, respectively.)

First, Figure 3.3 compares the normalized scaling factors computed from the numerical simulation with the theoretical ones described in Chapter 2. The comparison shows that the numerical and theoretical normalized scaling factors match well.

Next, Figure 3.4 compares the S_0 and A_0 modes decomposed by the proposed technique with the ones individually excited by the collocated PZTs A and C as shown in Figure 3.1. Here, the theoretical normalized scaling factors were used for the proposed mode decomposition technique. In the first column, the decomposed S_0 mode signal (the dashed line) is compared with the corresponding S_0 mode signal (the solid line) generated by exciting the collocated

PZTs A and C in-phase. Similarly, the decomposed A_0 signal is compared with the corresponding A_0 mode signal selected generated by exciting the collocated PZTs A and C out-of-phase. Due to limited space, the decomposition results obtained from only V_{13} and V_{23} are shown in Figure 3.4. The proposed technique successfully decomposes the S_0 and A_0 modes from V_{ij} so that the decomposed S_0 and A_0 modes match well with the selectively generated S_0 and A_0 modes using the collocated PZTs. It can be also seen that the reflections of the S_0 and A_0 modes as well as their first arrivals are effectively decomposed.

(a) S_0 modes in V_{13} (b) A_0 modes in V_{13}

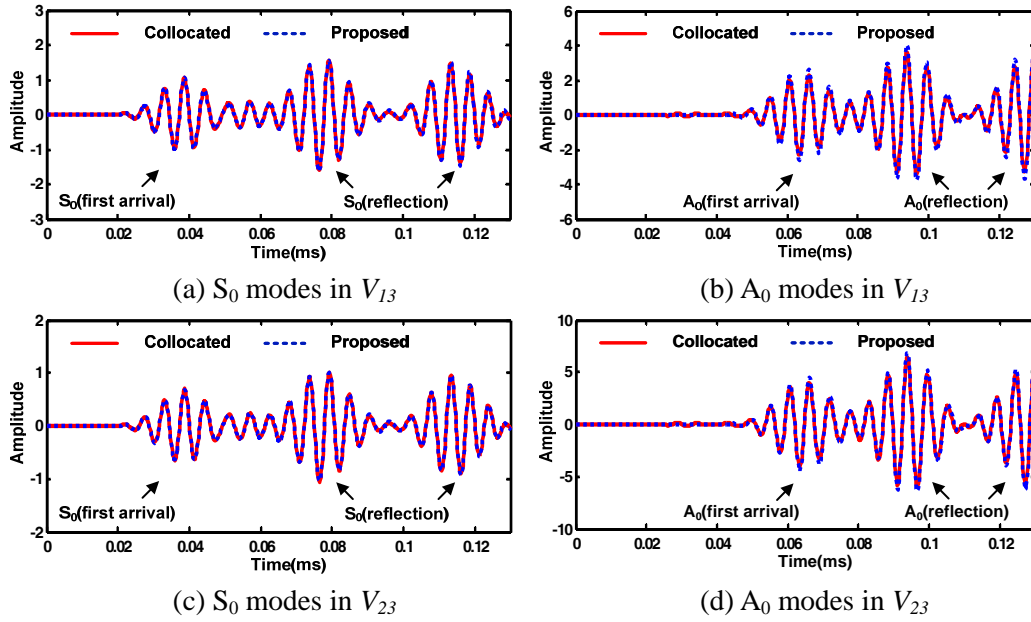(c) S_0 modes in V_{23} (d) A_0 modes in V_{23}

Figure 3.4 Comparison between the S_0 and A_0 modes decomposed by the proposed technique (the dashed line) and the ones selectively generated by the collocated PZTs A and C in Fig. 3 (the solid line): (a) the S_0 modes in V_{13}, (b) the A_0 modes in V_{13}, (c) the S_0 modes in V_{23}, and (d) the A_0 modes in V_{23}

CHAPTER 4
TEST RESULTS

4.1 Experimental setup

To further examine the feasibility of the proposed technique, experiments have been conducted on an aluminum plate. The dimension of the aluminum plate used in this study were 1000mm × 1000mm × 3mm and three identical dual PZTs were placed on the top of the plate and another identical dual PZT is placed on the other side of the plate shown in Figure 4.1. PZTs A and C are located at an identical position but attached on the different side. Note that PZT C is only used for the validation of the proposed technique and not needed for its actual implementation. Based on the theoretical velocities of the S_0 and A_0 modes at the driving frequency, the spacing between PZTs A and D was determined so that the first arriving S_0 mode is separated from the first arriving A_0 mode. On the other hand, PZT B was placed closer to PZT A so the S_0 and A_0 modes overlap.

The dual PZT used in this study was composed of circular and ring parts shown in Figure 4.2. In order to electrically isolate the dual PZT from the host structure and make wire connections to the dual PZTs easier, the dual PZTs are packaged with Kapton films.[28]

Figure 4.3 shows the data acquisition system used for the experiments. The data acquisition system consists of an arbitrary waveform generator (AWG), a

high speed signals digitizer (DIG), a low noise preamplifier (LNP), a power amplifier and multiplexers. Using the 14-bit AWG, a toneburst signal with a 12 peak-to-peak voltage and a driving frequency of 180 kHz was generated and applied. The driving frequency was selected to generate the S_0 and A_0 modes with similar amplitudes. The output voltage was filtered and amplified 50 times by the LNP, and measured by the DIG of which sampling rate and resolution were 20ms/s and 16 bits, respectively. The response signals were measured twenty times and averaged in the time domain to improve the signal-to-noise ratio.
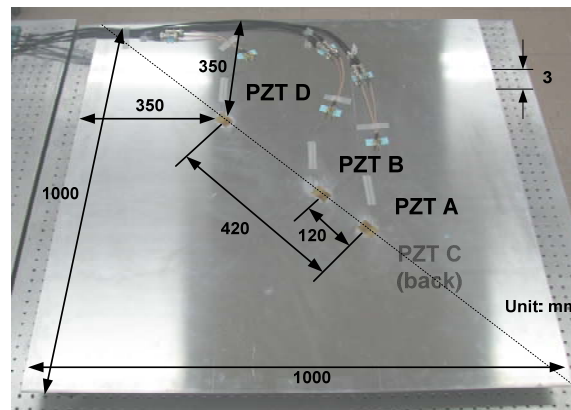
Figure 4.1 The configuration and dimension of the test specimen including four identical dual PZTs: PZTs A, B and D were installed on the top side of the plate and PZT C was located at the same position with PZT A but on the other side of the plate.
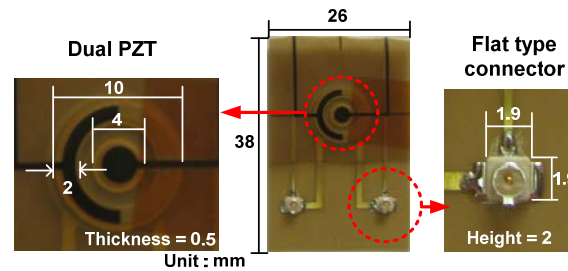
Figure 4.2 The dimension of the newly designed dual PZT with flat type connectors used in this study
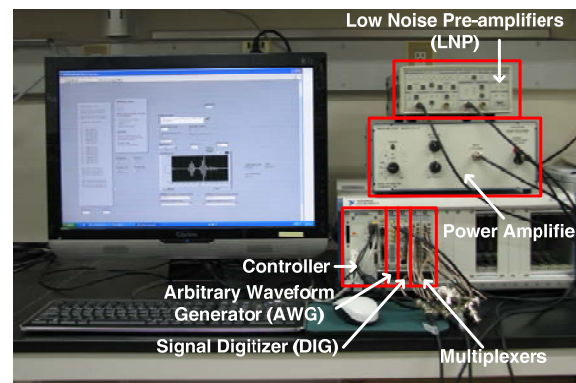

Figure 4.3 The data acquisition system used for the validation of the proposed technique
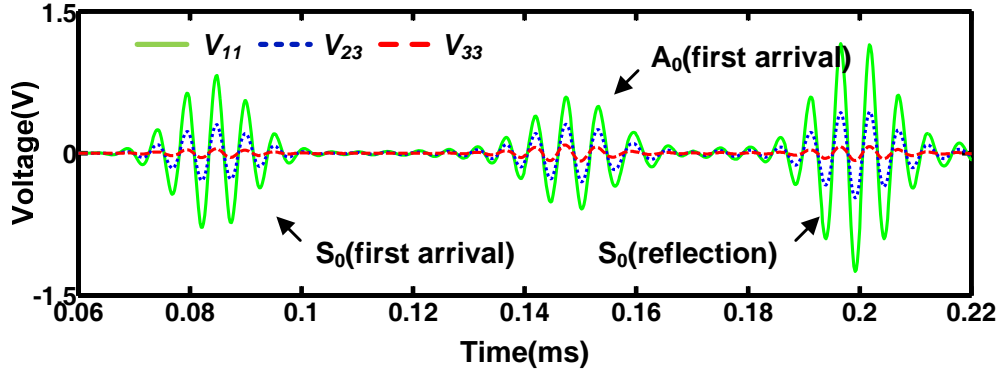
4.2 Experimental results

Figure 4.4 Comparison of V_{11}, V_{23} and V_{33} measured from the path AD: The S_0 and A_0 modes included in different V_{ij}'s have an identical arrival time but different amplitudes. (Due to limited space, only V_{11}, V_{23} and V_{33} out of nine V_{ij} are plotted.)

First, the effectiveness of the proposed technique is investigated using the path AD which has a longer spacing between excitation and sensing PZTs. Figure 4.4 shows V_{ij} measured from the path AD where the first arriving S_0 and A_0 modes are well separated. Here, the first three wave packets indicate the first arriving S_0 and A_0 and reflected S_0 modes from plate boundaries, respectively. As expected, the S_0 and A_0 modes in V_{11}, V_{23} and V_{33} have an identical arrival time but different amplitudes.

Once the normalized scaling factors are computed from the signed amplitudes of the first arriving S_0 and A_0 modes included in V_{ij}, the S_0 and A_0 modes are decomposed by following the procedure described in Chapter 2. Figure 4.5 compares the S_0 and A_0 modes in the path AD decomposed by the proposed

technique (the dashed line) with the S_0 and A_0 modes selectively excited (the solid line) by the collocated PZTs A and C as shown in Figure 4.1. For the generation of the S_0 and A_0 modes, collocated PZTs A and C were excited in-phase and out-of-phase, respectively. The test results show that the first arrivals and/or reflections of the S_0 and A_0 modes decomposed by the proposed are well agree with the selectively generated ones.

(a)   (b)

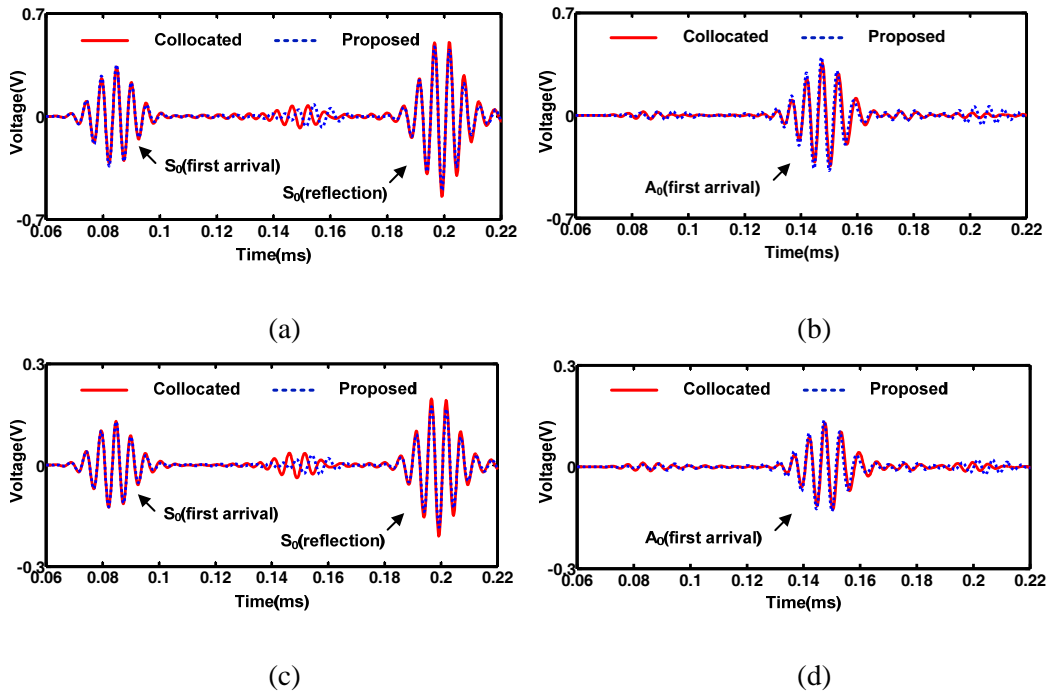(c)   (d)

Figure 4.5 Comparison between the S_0 and A_0 modes in the path AD decomposed by the proposed technique (the dashed line) and the ones selectively generated by the collocated PZTs A and C in Figure 4.1 (the solid line): (a) the S_0 modes in V_{13}, (b) the A_0 modes in V_{13}, (c) the S_0 modes in V_{32} and (d) the A_0 modes in V_{32}
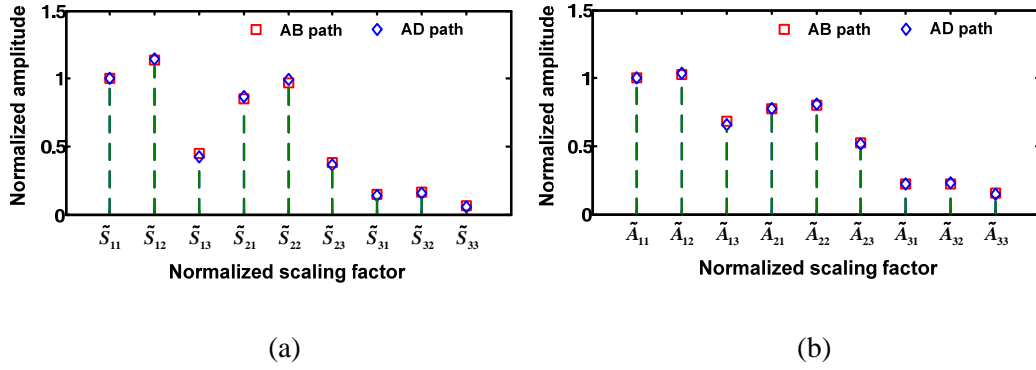
(a) (b)

Figure 4.6 Comparison of the normalized scaling factors of the S_0 and A_0 modes obtained from the paths AB and AD: (a) the S_0 mode and (b) the A_0 mode (The red rectangular and blue diamond indicate the normalized scaling factors from the paths AB and AD.)

Figure 4.6 shows that the normalized scaling factors in the path AD were in good agreement with those in the path AB where the first arriving S_0 and A_0 modes overlap. In theory, the normalized scaling factors should be identical among these two paths as long as the sizes of the used dual PZTs are identical. Thus, the S_0 and A_0 modes in the path AB can be decomposed using the normalized scaling factors obtained from the path AD even if the amplitudes of the S_0 and A_0 modes cannot be obtained from the path AB. Note that the normalized scaling factors in the AB path shown in Figure 4.6 were calculated from the amplitudes of the selectively generated S_0 and A_0 modes using collocated PZTs A and C. These normalized scaling factors from the collocated PZTs are used only for the comparison of the normalized scaling factors from the paths AD and AB. The actual mode decomposition of signals in the path AB is

accomplished using the normalized scaling factors estimated from the path AD.

Figure 4.7 shows the S_0 and A_0 modes at the path AB decomposed using the normalized scaling factors estimated from the path AD. The result shows that the decomposed S_0 and A_0 modes are in a good agreement with the selectively generated S_0 and A_0 modes signals. Even the first and/or second reflections of the S_0 and A_0 modes can be effectively extracted from the measured signals.
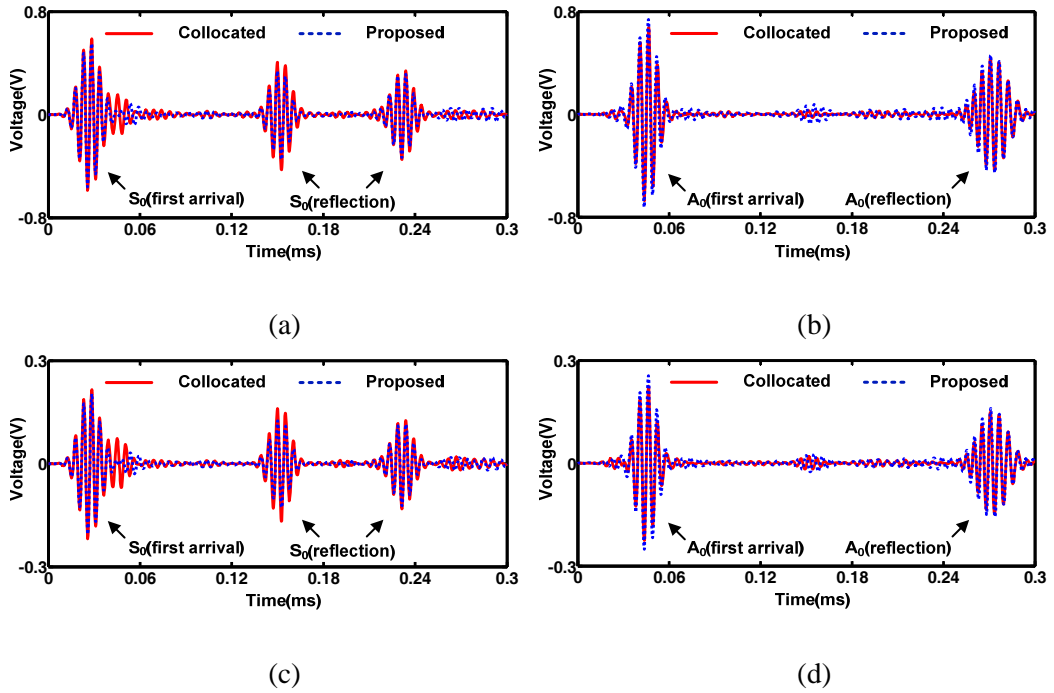

(a) (b)

(c) (d)

Figure 4.7 Comparison between the S_0 and A_0 modes in the path AB decomposed by the proposed technique (the dashed line) and the ones selectively generated by the collocated PZTs A and C in Figure 4.1 (the solid line): (a) the S_0 modes in V_{13}, (b) the A_0 modes in V_{13}, (c) the S_0 modes in V_{32} and (d) the A_0 modes in V_{32}

CHAPTER 7
CONCLUSION

In this study, a new Lamb wave decomposition technique is developed so that fundamental Lamb wave (S_0 and A_0) modes can be extracted from Lamb wave signals excited and measured by a pair of dual PZTs. The newly designed dual PZT consists of co-centered ring and circular PZTs, and multiple Lamb wave signals in a single wave path are generated and measured by activating different parts of the dual PZTs. Then, the mode decomposition is achieved through manipulating these multiple signals obtained from a pair of dual PZTs. The main advantage of the proposed decomposition technique is that both S_0 and A_0 modes can be decomposed at any desired frequency without any other special tuning such as the adjustment of the PZT size. Numerical simulation and experimental tests were conducted to validate the effectiveness of the proposed Lamb wave decomposition technique. Furthermore, since the scaling factors, necessary for the proposed decomposition technique can be instantaneously estimated from the target path or a reference path nearby, the proposed technique is expected to be less sensitive to changing temperature conditions. However, it should be noted that the proposed technique best operates under the following assumptions: (1) The target structure has a uniform thickness and isotropic material properties; (2) All the dual PZTs installed are identical in terms of their sizes and bonding conditions; (3) The driving frequency is selected so that only the S_0 and A_0 modes

are excited; and (4) Spatial distribution of temperature over the specimen is uniform although temperature variation over time is allowed and has no effect on the proposed technique. A further study is underway to extend the proposed concept to anisotropic structures and complex geometries with stiffeners or welded joints.

SUMMARY (IN KOREAN)

요　약　문

동심 원형 능동센서를 이용한 유도파의 모드 분해 기법

　　구조물 표면에 부착된 능동센서를 이용한 유도파 기반의 비파괴 검사 기법은 토목 구조물, 항공 구조물 및 기계 장비 등의 관리에 있어 경제적, 사회적 수요가 증가하고 있다. 유도파는 적은 감쇠율과 손상에 대해 민감한 반응 특성을 가지고 있기 때문에 구조물 안전 진단 검사 분야의 적용성을 인정받고 있다. 하지만 유도파의 분산 및 다중 모드 특성으로 인하여 신호 해석 시 어려움을 겪게 된다. 이를 해결하기 위해 동심 원형 능동센서를 이용한 새로운 개념의 모드 분해 기법을 개발하였다. 기존 기법은 능동 센서를 양면에 붙이거나 모드 분해를 특정 주파수나 정해진 능동 센서 크기에서만 이용 가능 하였다. 하지만 제안된 방법은 동심형 능동 센서를 이용하여 가진 주파수 및 크기에 상관없이 구조물의 한쪽 면에만 센서를 부착하여 모드 분해를 가능케 하게 하였다. 이를 위해 동심 원형 능동 센서의 3D 유도파 전파를 공식화 하였고 수치 해석 및 알루미늄 패널을 이용한 실험을 통해 유효성및 적용성을 검증 하였다. 본 실험에 사용된 유한 요소법 수치해석 프로그램으로는 MD/NASTRAN이 사용되었으며 PATRAN 2010을 통해 결과를 분석하였다. 실 구조물의 적용성을 확인하기 위해 상용적으로 이용되는 알류미늄 판넬을 이용하여 실험을 수행하였다.

REFERENCES

[1] D. Alleyne and P. Cawley, "The interaction of Lamb waves with defects," IEEE Trans. Ultrason. Ferroelectr. Freq. Control **39**, 381–397 (1992).

[2] M. J. Lowe, P. Cawley, J. Y. Kao, and O. Diligent, "The low frequency reflection characteristics of the fundamental antisymmetric Lamb wave a_0 from a rectangular notch in a plate," J. Acoust. Soc. Am. **112**, 2612–2622 (2002).

[3] A. Raghavan and C. E. S. Cesnik, "Review of guided-wave structural health monitoring," Shock Vib. Dig. **39**, 91–114 (2007).

[4] M. J. Lowe and O. Diligent, "Low frequency reflection characteristics of the S_0 Lamb wave from a rectangular notch in a plate," J. Acoust. Soc. Am. **111**, 64–74 (2002).

[5] S. S. Kessler, S. M. Spearing, and C. Soutis, "Damage detection in composite materials using Lamb wave methods," Smart Mater. Struct. **11**, 269–278 (2002).

[6] Z. Su, L. Ye, and Y. Lu, "Guided Lamb waves for identification of damage in composite structures: A review," J. Sound Vib. **295**, 753–780 (2006).

[7] V. Giurgiutiu, *Structural Health Monitoring: with Piezoelectric Wafer Active Sensors* (Academic Press, San Diego, CA, 2008).

[8] E. Moulin, J. Assaad, C. Delebarre, H. Kaczmarek, and D. Balageas, "Piezoelectric transducer embedded in a composite plate: application to Lamb wave generation," J. Appl. Phys. **82**, 2049-2055 (1997).

[9] F. L. di Scalea, H. Matt, and I. Bartoli, "The response of rectangular piezoelectric sensors to Rayleigh and Lamb ultrasonic waves," J. Acoust. Soc. Am. **121**, 175–187 (2007).

10. S. R. Anton, D. J. Inman, G. Park, "Reference-Free damage detection using instantaneous baseline measurements," AIAA Journal **47**, 1952-1964 (2009).

11. S. B. Kim, and H. Sohn, "Instantaneous reference-free crack detection based on polarization characteristics of piezoelectric materials," Smart Mater. Struct. **16**, 2375-2387 (2007).

12. J. B. Ihn and F. K. Chang, "Detection and monitoring of hidden fatigue crack growth using a built-in piezoelectric sensor/actuator network: I. diagnostics," Smart Mater. Struct. **13**, 609–620 (2004).

13. P. D. Wilcox, M. J. S. Lowe, and P. Cawley, "Mode and transducer selection for long range Lamb wave inspection," J. Intell. Mater. Syst. Struct. **12**, 553–565 (2001).

14. M. Castaings and P. Cawley, "The generation, propagation, and detection of Lamb waves in plates using air-coupled ultrasonic transducers," J. Acoust. Soc. Am. **100**, 3070–3077 (1996).

15. I. A. Viktorov, *Rayleigh and Lamb Waves* (Plenum, New York, 1967).

16. J. L. Rose, S. P. Pelts, and M. J. Quarry, "A comb transducer for mode control in guided wave NDE," IEEE Ultras. Symp. Proc. 857–860 (1996).

17. F. L. Degertekin and B. T. Khuri-Yakub, "Single mode lamb wave excitation in thin plates by Hertzian contacts," Appl. Phys. Lett. **69**, 146–148 (1996).

18. K. Yamanaka, Y. Nagata and T. Koda, "Selective excitation of single-mode acoustic waves by phase velocity scanning of a laser beam," Appl. Phys. Lett. **58**, 1591-1593 (1991).

19. Z. Su, L. Ye, "Selective generation of Lamb wave modes and their propagation characteristics in defective composite laminates," J. Mater: Des. Appl. **218**, 95-110 (2004).

20. S. C. Wooh and Y. J. Shi, "Synthetic phase tuning of guided waves," IEEE Trans. Ultrason. Ferroelectr. Freq. Control **48**, 209–223 (2001).

21. F. L. di Scalea, H. Matt, and I. Bartoli, "The response of rectangular piezoelectric sensors to Raleigh and Lamb ultrasonic waves," J. Acoust. Soc. Am. **121**, 175–187 (2007).

22. G. B. Santoni, L Yu, B. Xu, V. Giurgiutiu, " Lamb wave-mode tuning of piezoelectric wafer active sensors for structural health monitoring," J. Vib. Acoust. **129**, 752-762 (2007).

23. A. Raghavan and C. E. S. Cesnik, "Finite-dimensional piezoelectric transducer modeling for guided wave based structural health monitoring," Smart Mater. Struct. **14**, 1448-1461 (2005).

24. H. Sohn, S. J. Lee, "Lamb wave tuning curve calibration for surface-bonded piezoelectric transducers," Smart Mater. Struct. **19**, 015007 (2010).

25. G. N. Watson, *A Treatise on the Theory of Bessel Functions*, 2nd ed. (Cambridge U. P., London, 1958).

26. S. S. Kessler and D. J. Shim, "Validation of a Lamb Wave-Based Structural Health Monitoring System for Aircraft Applications," *Proc. SPIE Smart Structures/NDE Joint Conference,* San Diego, CA, Paper No. 293-301 (2005).

27. Anonymous, MSC.NASTRAN User Guide.

28. http://www.metisdesign.com(date last viewed 4/21/10)

감사의 글

CURRICULUM VITAE

Chulmin Yeum

Research Assistant

The Civil and Environmental Engineering Department

Korea Advanced Institute of Science and Technology

373-1 Guseong-dong, Yuseong-gu

Daejeon, Republic of Korea, 305-701

Office: (82)+42-869-3665, Fax: (82)+42-869-3610

Email: chulminy@gmail.com

RESEARCH INTERESTS

Real-time Structural Health Monitoring System for Current and Future Composite Vehicles.
Damage Detection on Composite and Metallic Structures
Probabilistic Image Construction
Finite element modeling(FEM)

EDUCATION

2008-2010	**M.S.**, Civil Eng., Korea Advanced Institute of Science and Technology (KAIST), KOREA.
2002-2008	**B.S.**, Civil Eng., Korea Advanced Institute of Science and Technology (KAIST), KOREA.

PARTICIPANT PROJECTS

2008-present	**On-board SHM technologies for composite air vehicles (Research Assistant)**: The Boeing Company(Funded: $400,000 for 09/05/08 to 08/01/11)
2008	**Undergraduate Research Program (Primary Researcher) :** Application of reference-free damage detection to composite aircraft structures: probabilistic damage localization using embedded piezoelectric sensor network funded by KAIST (Funded: $5,000 for 08/03/02 to 08/06/02)

EDUCATIONAL EXPERIENCES

Spring 2010	**Teaching Assistant**, CE580, "Statistical Pattern Recognition for Structural Health Monitoring," (undergraduate level course), KAIST, Korea, 3 unit graduate course
Fall 2009	**Research Assistant, Undergraduate Research Program (URP),** A program that supports undergraduate student research in a practical way through research funding and credit point attainment for undergraduate students of KAIST. The research topic is "Stress analysis of bolted joint" conducted by Seo Young Hwan.
Fall 2008	**Research Assistant, Undergraduate Research Program (URP),** A program that supports undergraduate student research in a practical way through research funding and credit point attainment for undergraduate students of KAIST. The research topic is "Theoretical modeling for A_0 Lamb wave reflection and transmission at a finite vertical discontinuity using Eigen-mode method" conducted by Lim Hyung Jin.
Spring 2008	**Teaching Assistant**, CE207, "Elementary structural Engineering & Laboratory," (undergraduate level course), KAIST, Korea. 3 unit undergraduate course.

EXPERIMENTAL EXPERIENCES

2010	**Installation of sensors on a composite aircraft**, The DACC Company, Wanju, KOREA : Real time monitoring of composite air vehicles funded by Korean Agency for Defense Development (ADD)
2009	**Field monitoring of real bridge structures**, Kimpo(Kimpo bridge) & Icheon (Samseung bridge), KOREA : US-Korea collaborative research for bridge monitoring testbeds

JOURNAL PUBLICATIONS

* The corresponding author is underlined.

1. **<u>Chulmin Yeum</u>**, Hoon Sohn* and Jeong Beom Ihn, "Reference-free delamination detection and localization in a composite plate using a dual piezoelectric transducer network," In preparation for Composites Structures, 2010. (Impact factor: 2.53)
2. **<u>Chulmin Yeum</u>**, Hoon Sohn* and Jeong Beom Ihn, "Lamb wave mode decomposition using concentric ring and circular PZT Transducers," Submitted to Journal of Acoustical Society of America, 2010. (Impact factor: 2.018)

CONFERENCE PROCEEDINGS

* The corresponding author is underlined.

1. **<u>Chulmin Yeum</u>**, Hoon Sohn*, Jeon Beom Ihn, "Lamb Wave Decomposition using Amplitude Matching with Concentric Circular PZT Transducers," the 5th European Workshop on Structural Health Monitoring, Sorrento, Italy, June 29-July 02, 2010.
2. **<u>Chulmin Yeum</u>**, Hoon Sohn*, "Probabilistic damage localization using embedded piezoelectric sensor networks" ,*the 2th UiTM-KAIST symposium on Urban Engineering and Sustainability,* Daejon, Korea , March 31 ,2008
3. Hoon Sohn*, Seung Bum Kim, Chang Gil Lee, **<u>Chulmin Yeum</u>**, Jeong Bum Ihn, "Reference-Free Delamination Detection in Multilayer Composite Panels," *Multi-Functional Materials and Structures,* Hong Kong, China, July 28-31, 2008.
4. Hoon Sohn*, Seung Bum Kim, Sang Jun Lee, Debaditya Dutta, Hyun Jun Park, Chang Gil Lee, Abhinav Agrawal, **<u>Chulmin Yeum</u>**, Seung Hee Park, Yun Kyu An, "Transition from Guided Wave Based Non-Destructive Testing to Structural Health Monitoring," 35th Annual Review of Progress in Quantitative Nondestructive Evaluation (QNDE 2008), Chicago, IL, July 20-25, 2008.

HONORS & AWARDS

Undergraduate Research Program Award (2008): Under Prof. Sohn supervision, I was awarded with the Third Prize for the winter/spring undergraduate research program at KAIST in 2008 for his project entitled "Application of reference-free damage detection to composite aircraft structures: probabilistic damage localization using embedded piezoelectric sensor network".

Scholarships for outstanding students granted KAIST (2005-2008): The three prominent students in the civil engineering department of KAIST were selected as recipients. This scholarship provided 2000$ per year for three years.

PATENT & COPYRIGHT

Hoon Sohn, **<u>Chulmin Yeum</u>**, Jeong Bum Ihn, "A lamb wave mode decomposition technique using amplitude matching," Submitted to the Us patent office, Docket No. 09-0869.

SKILLS

Program : MATALB, FORTRAN, NASTRAN, PATRAN,COMSOL,
Equipments : Multi Channel Data Acquisition Systems.(National Instruments
Digital Signal Processing